Lagrangian Coherent Structures in the Elliptic Restricted Three-Body Problem

Evan Gawlik

SURF 2007 Final Report
Mentor: Dr. Jerrold E. Marsden, Control and Dynamical Systems, Caltech
Co-Mentor: Philip Du Toit, Control and Dynamical Systems, Caltech

Abstract

This study investigates Lagrangian coherent structures (LCS) in the elliptic restricted three-body problem (ER3BP), a generalization of the circular restricted three-body problem (CR3BP) that asks for the motion of a test particle in the presence of two elliptically orbiting point masses. Previous studies demonstrate that an understanding of transport phenomena in the CR3BP, an autonomous dynamical system, can be obtained through analysis of the stable and unstable manifolds of certain periodic solutions to the CR3BP equations of motion. These invariant manifolds form cylindrical tubes within surfaces of constant energy that act as separatrices between orbits with qualitatively different behaviors. The computation of LCS, a technique typically applied to fluid flows to identify transport barriers in the domains of time-dependent velocity fields, provides a convenient means of determining the time-dependent analogues of these invariant manifolds for the ER3BP, whose equations of motion contain an explicit dependency on the independent variable. As a direct application, this study uncovers the contribution of elliptically orbiting mass pairs to the Interplanetary Transport Network, a network of tubes through the solar system that can be exploited for the construction of low-fuel spacecraft mission trajectories.

1 Introduction

The three-body problem is a dynamical system rich in mathematical intricacy and practical applicability. A classic problem in the study of celestial mechanics, the general three-body problem asks for the motion of three masses in space under mutual gravitational interaction. The benefit to investigating the three-body problem is twofold: results of such studies often bear broader implications in the theory of dynamical systems, and the investigations themselves are patently well-suited to address challenges in astronomy. In particular, obtaining a global picture of the dynamical barriers that govern the transport of material through a celestial system is an issue of import to scientists in a surprisingly wide range of fields[1,2]. The study applies the theory of Lagrangian coherent structures outlined by Shadden et al.[3] to determine transport barriers in the elliptic restricted three-body problem (ER3BP).

Koon and co-authors[4] demonstrate that an understanding of transport phenomena in the circular restricted three-body problem (CR3BP), a problem that asks for the motion of a test particle in the presence of two circularly orbiting point masses, can be obtained through investigation of the stable and unstable manifolds—sets of points in the system's phase space that tend toward a given limiting set as time tends to plus or minus infinity—of certain periodic solutions to the three-body problem equations of motion. Evidently, a globalization of the stable and unstable manifolds of periodic orbits about the L_1 and L_2 Lagrange points (unstable equilibrium points in the the CR3BP) reveals a web of tubes through phase space that form separatrices between its dynamically different regions. This labyrinth of tubes, dubbed an "Interplanetary Transport Network"[5], can be exploited in a variety of ways, including a furthering of our understanding of unusual comet trajectories[6], the investigation of transport of material throughout the solar system[7], and the construction of orbits with prescribed itineraries for low-fuel spacecraft mission trajectories[8].

Computational methods for determining the invariant manifolds of dynamical systems are well-developed for autonomous systems of differential equations like those describing the CR3BP[9]. When we turn our
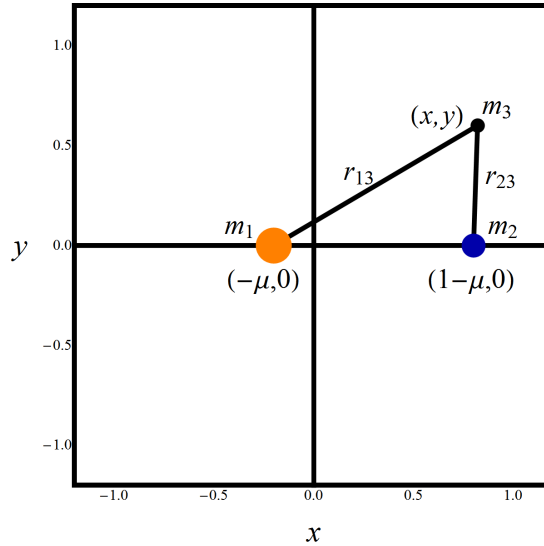
Figure 1: Rotating coordinate system in the circular restricted three-body problem. All units are nondimensionalized. The coordinate frame rotates counterclockwise with unit angular frequency. In the case of the elliptic restricted three-body problem, the picture is the same, but the frame rotates nonuniformly and pulsates isotropically in x and y to ensure that the primary masses remain fixed at the positions $(-\mu, 0)$ and $(1 - \mu, 0)$.

attention to non-autonomous differential equations (where velocity fields are time-dependent), the methods available for computing stable and unstable manifolds are no longer applicable, as the notions of stable and unstable manifolds for time-dependent vector fields are not even well-defined. Such is the case in the elliptic restricted three-body problem, where no choice of reference frame can rid the differential equations of motion of their time dependency. However, Shadden and co-authors[3] shed light on this issue in their development of the theory of Lagrangian coherent structures (LCS) for time-dependent flows. In their report, the authors provide a rigorous justification that LCSs–transport barriers in the domain of a time-dependent velocity field that can be computed algorithmically–"represent nearly invariant manifolds even in systems with arbitrary time dependence" under suitable conditions[3].

1.1 The Restricted Three-Body Problem

1.1.1 The Circular Restricted Three-Body Problem (CR3BP)

The circular restricted three-body problem (CR3BP) considers the motion of a test mass $m_3 = 0$ in the presence of the gravitational field of two primary masses $m_1 = 1 - \mu$ and $m_2 = \mu$ in circular orbit about their center of mass. Throughout this report, the test particle is assumed to begin in the orbital plane of the two primary masses with its velocity component normal to that plane equal to zero, so that its motion is constrained to the m_1-m_2 orbital plane for all time. Without loss of generality, all units are normalized and positions are defined relative to a rotating coordinate frame whose x-axis coincides with the line joining m_1 and m_2 and whose origin coincides with the center of mass of m_1 and m_2, as shown in Fig. 1. The equations of motion for the test particle are then[10]

$$\ddot{x} - 2\dot{y} = \frac{\partial \Omega}{\partial x} \tag{1}$$

$$\ddot{y} + 2\dot{x} = \frac{\partial \Omega}{\partial y}, \tag{2}$$

where

$$\Omega(x, y) = \frac{x^2 + y^2}{2} + \frac{1 - \mu}{\sqrt{(x + \mu)^2 + y^2}} + \frac{\mu}{\sqrt{(x - 1 + \mu)^2 + y^2}} + \frac{1}{2}\mu(1 - \mu) \tag{3}$$
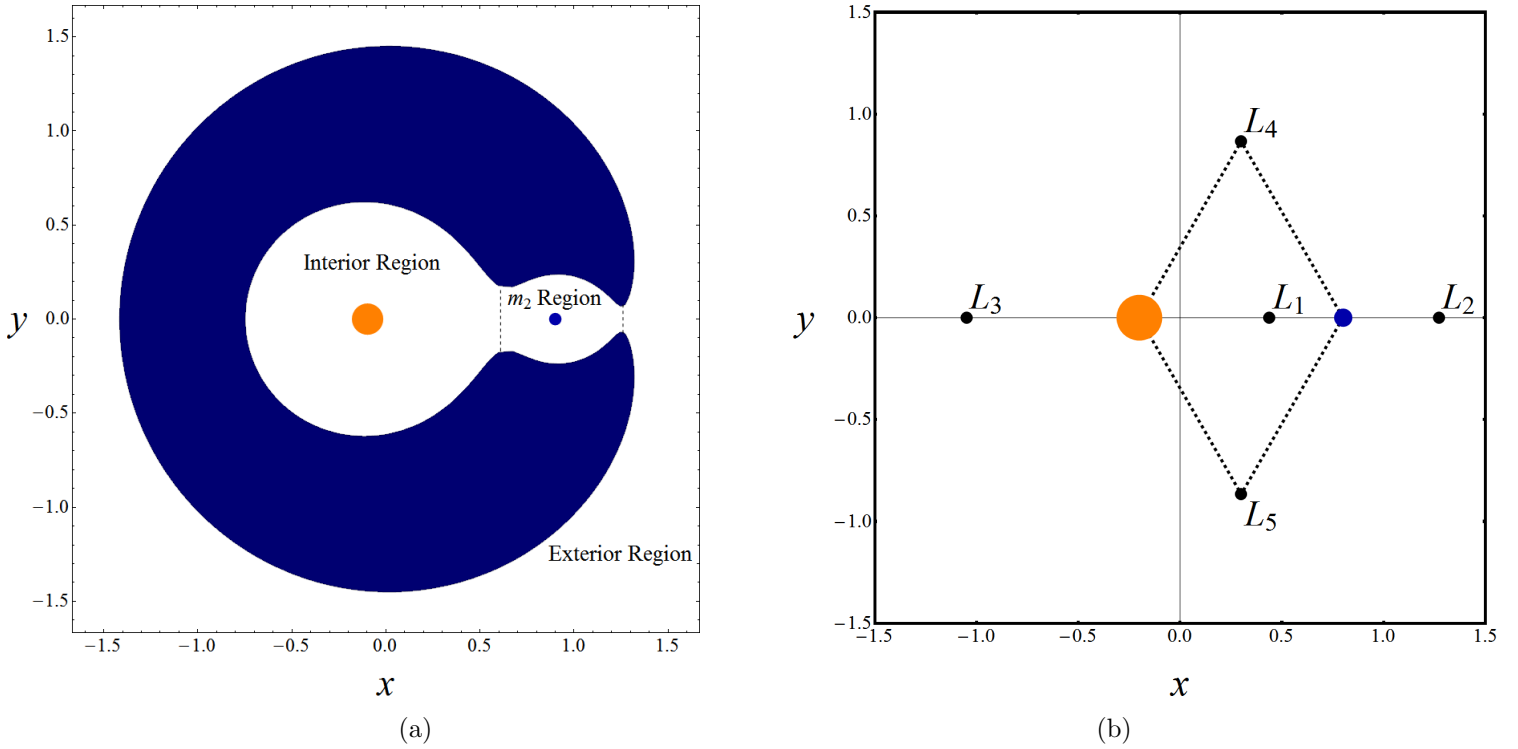
Figure 2: (a) Regions of allowed motion (white areas) in the circular restricted three-body problem with $\mu = 0.1$, $E = -1.775$. (b) Equilibrium points L_i, $i = 1, 2, 3, 4, 5$ in the circular restricted three-body problem with $\mu = 0.1$.

and (x, y) denotes the position of m_3 in the rotating frame. This system possesses two degrees of freedom, which implies that its phase space is four dimensional; four coordinates (x, y, $\dot{x}$, and $\dot{y}$, for instance) are required to specify an initial condition that corresponds to a unique trajectory.

There are five equilibrium points in the CR3BP[10], corresponding to critical points of the effective potential Ω. A particle placed at one of these points, which shall be referred to as the Lagrange points L_i, $i = 1, 2, 3, 4, 5$, will remain there for all time provided its initial velocity is zero with respect to the rotating frame. Three of these Lagrange points (L_1, L_2, and L_3) are collinear with the masses m_1 and m_2, while the remaining two (L_4 and L_5) lie at the vertices of the pair of equilateral triangles whose bases coincide with the line segment joining m_1 and m_2 (see Fig. 2(b)). Let L_i^x and L_i^y denote the x and y coordinates, respectively, of ith Lagrange point.

It is straightforward to check through differentiation that

$$E(x, y, \dot{x}, \dot{y}) = \frac{1}{2}(\dot{x}^2 + \dot{y}^2) - \Omega(x, y) \tag{4}$$

is a constant of motion for the CR3BP. We shall refer to this constant as the energy of the system, taking care not to confuse E with the sum of the test particle's kinetic and potential energies. Throughout this report, $E(L_i)$ shall denote the energy of the ith Lagrange point, i.e. $E(L_i) = E(L_i^x, L_i^y, 0, 0)$. Since E is constant in the CR3BP and $(\dot{x}^2 + \dot{y}^2)$ is a nonnegative quantity, it immediately follows that m_3 is restricted to regions of the (x, y) plane where

$$-\Omega(x, y) \leq E. \tag{5}$$

Moreover, a given particle in the CR3BP is constrained to a three-dimensional energy surface $\mathcal{M} = \{(x, y, \dot{x}, \dot{y}) \mid E(x, y, \dot{x}, \dot{y}) = const.\}$ defined by its initial energy.
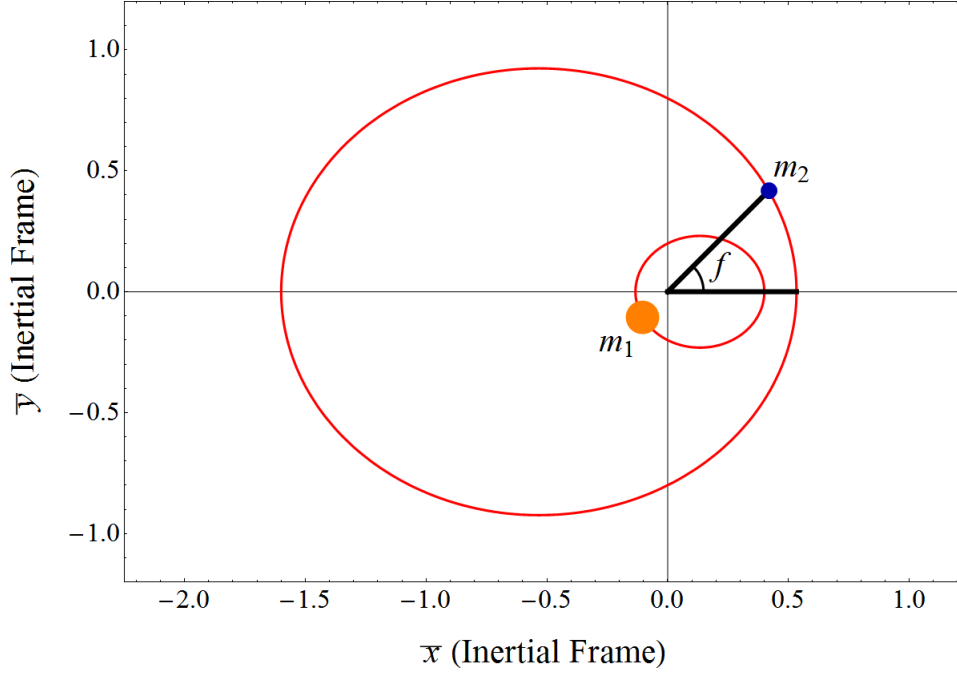
Figure 3: Elliptical orbits of the primary masses m_1 and m_2 in the ER3BP with respect to an inertial barycentric frame for the case $e = 0.5$, $\mu = 0.2$.

1.1.2 The Elliptic Restricted Three-Body Problem (ER3BP)

A natural generalization of the CR3BP is the elliptic restricted three-body problem (ER3BP), which asks for the motion of a test particle in the presence of two *elliptically* orbiting point masses. In the ER3BP, we introduce the true anomaly $f(t)$, the angle that the line segment joining the rightmost focus of m_2's elliptical orbit to m_2's position at periapsis makes with the line segment joining that focus to m_2's position at time t (see Fig. 3). Normalizing units so that the pair of primary masses has unit angular momentum and the distance between the two primaries at $f = \frac{\pi}{2}$ is unity, it follows from the general solution to the two-body problem [11] that m_1 and m_2 trace out ellipses given parametrically by

$$(\bar{x}_{m_1}, \bar{y}_{m_1}) = (\frac{-\mu}{(1 + e \cos f)} \cos f, \frac{-\mu}{(1 + e \cos f)} \sin f) \tag{6}$$

$$(\bar{x}_{m_2}, \bar{y}_{m_2}) = (\frac{1 - \mu}{(1 + e \cos f)} \cos f, \frac{1 - \mu}{(1 + e \cos f)} \sin f), \tag{7}$$

where $(\bar{x}_{m_i}, \bar{y}_{m_i})$, $i = 1, 2$ is the position of ith primary mass with respect to an inertial, barycentric coordinate frame.

It can then be shown, as is done in Section 4, that if the true anomaly f is designated the independent variable of the system, then the equations of motion for the elliptic restricted three-body problem take the form

$$\frac{d^2 x}{df^2} - 2 \frac{dy}{df} = \frac{\partial \Omega}{\partial x} \Big/ (1 + e \cos f) \tag{8}$$

$$\frac{d^2 y}{df^2} + 2 \frac{dx}{df} = \frac{\partial \Omega}{\partial y} \Big/ (1 + e \cos f), \tag{9}$$

where e is the eccentricity of m_2's elliptical orbit (which is identical to that of m_1's orbit), and x and y are the coordinates of m_3 in a nonuniformly rotating, isotropically pulsating, barycentric coordinate frame in which m_1 and m_2 have fixed positions $(-\mu, 0)$ and $(1 - \mu, 0)$, respectively. We shall treat the variable f as the "time" in the ER3BP, but, to avoid ambiguity, shall use primes to denote differentiation with respect
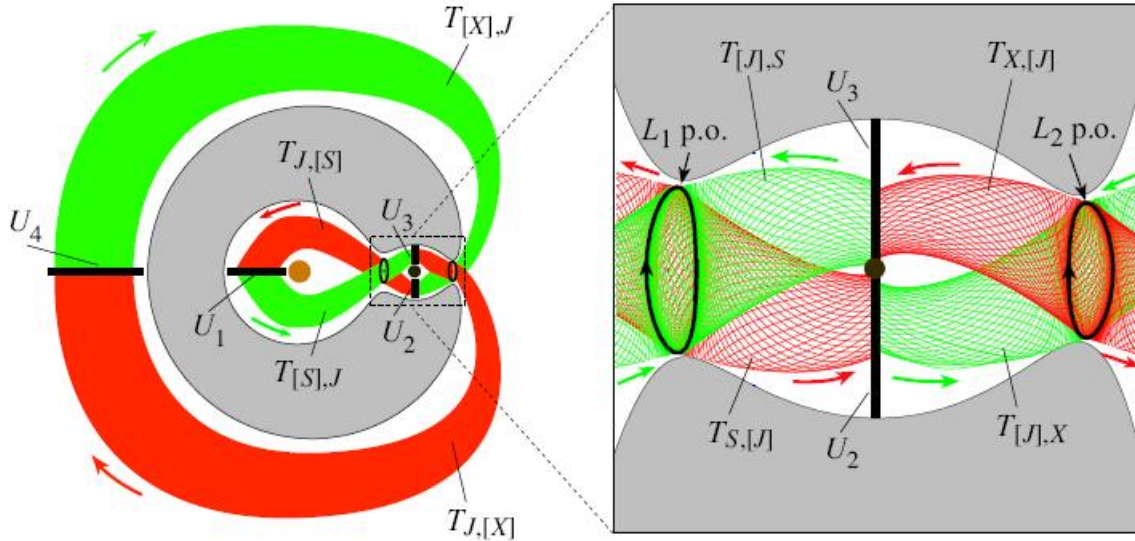
Figure 4: Projection of the stable (green) and unstable (red) manifold tubes in the CR3BP onto position space. Image borrowed from Koon *et al.*[4]

to f and dots to denote differentiation with respect to t. Note that when $e = 0$, our choice of units give $f = t$ so that equations (8-9) reduce to the equations of motion (1-2) of the circular restricted three-body problem. Thus, the CR3BP is the special case of the ER3BP in which the two primary masses have zero orbital eccentricity.

1.2 Invariant Manifolds

The presence of forbidden regions in the CR3BP permits the definition of three subsets of the (x, y) plane when $E(L_2) < E < E(L_3)$: the interior, m_2, and exterior regions, bounded approximately by the lines $x = L_1^x$, $x = L_2^x$, and the boundary of the forbidden regions (see Fig. 2(a)). A natural question to pose now is the following: What regulates the transport of particles between the interior, m_2, and exterior regions in the CR3BP?

Koon and co-authors[4] provide the answer to this question through analysis of the invariant manifolds of periodic orbits in the CR3BP. By linearizing the equations of motion at the collinear Lagrange points, the authors show that these equilibrium points have the stability type *saddle* × *center*. Consequently, there exists a family of periodic orbits (called Lyapunov orbits) about L_i for each $i \in 1, 2, 3$, whose stable and unstable manifolds form cylindrical tubes ($S^1 \times \mathbb{R}$). Moreover, within a surface of constant energy, these tubes (as shown in Fig. 4) form codimension-1 separatrices between orbits with different fates: transit orbits, which exit one region and enter an adjacent region; and non-transit orbits, which remain entrapped in the region in which they began. More precisely, a particle with energy E that is currently in a given region R_A will enter an adjacent region R_B under the forward (respectively, backward) time flow if and only if that particle is inside the stable (respectively, unstable) manifold tube emanating from the unique periodic orbit of energy E associated with the Lagrange point that lies on the shared boundary of regions R_A and R_B.

Computational methods for determining the CR3BP invariant manifolds are well-developed[9,12]. To sumarize the procedure, one first constructs a periodic orbit with a specified energy using differential correction, a method akin to Newton's method for finding roots of nonlinear expressions. The evolution of the periodic orbit's state transition matrix (the derivative of the flow with respect to initial position) is computed over one period, and local approximations of the stable and unstable manifolds of the periodic orbit are obtained from the eigenvectors of that state transition matrix. A set of tracers in the directions of the stable and unstable eigenspaces can then be advected under the full nonlinear equations of motion to generate the
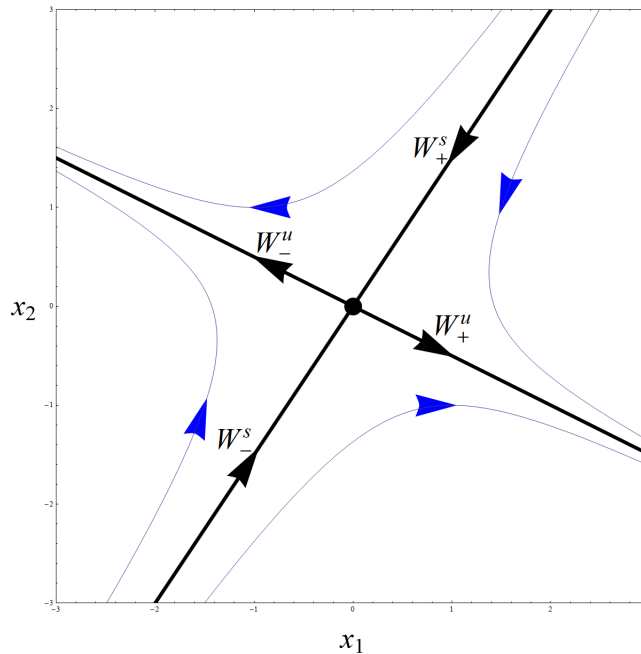
Figure 5: Phase portrait for an autonomous linear dynamical system with a saddle point at the origin. The origin's stable manifold forms a separatrix between trajectories that tend toward oppositely directed halves of the unstable manifold.

invariant manifolds. The process can be curtailed by exploiting a symmetry in the CR3BP equations of motion: the mapping $(x, y, \dot{x}, \dot{y}, t) \mapsto (x, -y, -\dot{x}, \dot{y}, -t)$ is a symmetry of equations (1-2); as a result, the unstable manifold of a given Lyapunov orbit can be found by negating the y and $\dot{x}$ coordinates of every point on the corresponding stable manifold.

1.3 Lagrangian Coherent Structures (LCS)

The invariant manifolds of the CR3BP are associated with periodic solutions to the time-independent equations of motion (1-2). In a non-autonomous dynamical system like the ER3BP, the existence of exactly periodic motion disintegrates, as does the presence of static invariant manifolds. Fortunately, the theory of Lagrangian coherent structures (LCS) generalizes the notions of stable and unstable manifolds to non-autonomous dynamical systems[3].

To motivate the definition of an LCS, consider an autonomous dynamical system $\dot{\mathbf{x}} = A\mathbf{x}$, $\mathbf{x} = (x_1, x_2)^T$, with A a constant matrix possessing two real eigenvalues opposite in sign[1], as in Fig. 5. Let Φ be the flow of the dynamical system. The unstable manifold of the fixed point consists of two halves, W_+^u and W_-^u, emanating from the origin in opposite directions. One can then partition the plane into two regions with dynamically different fates: $R_+ = \{\mathbf{x} \in \mathbb{R}^2 \mid \Phi^t(\mathbf{x}) \to W_+^u \text{ as } t \to \infty\}$ and $R_- = \{\mathbf{x} \in \mathbb{R}^2 \mid \Phi^t(\mathbf{x}) \to W_-^u \text{ as } t \to \infty\}$. The boundary separating R_+ from R_- is precisely the stable manifold W^s. Any two particles placed on opposite sides this separatrix, regardless of their initial separation distance, eventually achieve a large separation distance that grows without bound. Guided by this intuition, we can identify the stable manifold as a curve of high stretching under the forward time flow. Likewise, the unstable manifold corresponds to a curve of high stretching under the backward time flow.

To characterize this stretching, consider a general initial value problem

$$\dot{\mathbf{x}}(t) = \mathbf{v}(\mathbf{x}, t) \tag{10}$$

$$\mathbf{x}(t_0) = \mathbf{x}_0 \tag{11}$$

---

[1]In actuality, any efforts to study Lagrangian coherent structures in a linear system such as this would be in vain, as the state transition matrix for this system is independent of initial position. Nevertheless, qualitative observations of saddle points provide a solid foundation upon which to build an intuition for LCS.

with a velocity field $\mathbf{v}(\mathbf{x}, t)$ defined on some domain $D \subseteq \mathbb{R}^n$. Let $\Phi_{t_0}^t : D \to D$ be the flow of the differential equation (10). Then the separation between two trajectories $\mathbf{x}(t)$ and $\mathbf{y}(t)$ with neighboring initial conditions $\mathbf{x}(t_0) = \mathbf{x_0}$ and $\mathbf{y}(t_0) = \mathbf{x_0} + \delta \mathbf{x_0}$ will at time $t_0 + T$ be given by

$$\mathbf{y}(t_0 + T) - \mathbf{x}(t_0 + T) = \frac{d\Phi_{t_0}^{t_0+T}(\mathbf{x})}{d\mathbf{x}} \delta \mathbf{x_0} + \mathcal{O}(||\delta \mathbf{x_0}||^2). \tag{12}$$

Observing that the spectral norm of the linearization of $\Phi_{t_0}^{t_0+T}(\mathbf{x})$ about $\mathbf{x} = \mathbf{x_0}$ provides an indication of the maximum extent to which the two trajectories diverge after the elapsed time T, it makes sense to define a number

$$\sigma_{t_0}^T(\mathbf{x}) = \frac{1}{|T|} \ln \left| \left| \frac{d\Phi_{t_0}^{t_0+T}(\mathbf{x})}{d\mathbf{x}} \right| \right| \tag{13}$$

to serve as a measure of the exponential divergence of trajectories with neighboring initial conditions. Here, $\left| \left| \frac{d\Phi_{t_0}^{t_0+T}(\mathbf{x})}{d\mathbf{x}} \right| \right|$ denotes the square root of the largest eigenvalue of the matrix

$$\Delta = \frac{d\Phi_{t_0}^{t_0+T}(\mathbf{x})}{d\mathbf{x}}^* \frac{d\Phi_{t_0}^{t_0+T}(\mathbf{x})}{d\mathbf{x}}. \tag{14}$$

Computation of this so-named finite-time Lyapunov exponent (FTLE) for a grid of initial positions $\mathbf{x}(t_0)$ within the domain of the dynamical system yields a scalar field from which ridges (curves—or, more generally, codimension-1 surfaces in systems with arbitrary dimension—in the domain whose images in the graph of the FTLE field satisfy certain conditions that formalize intuitive notions of a ridge; see Lekien *et al.*[13] for details) can be extracted for a range of initial times t_0. These time-varying ridges, which form barriers between the almost invariant sets of the domain, are the sought-after LCSs.

Observe that (13) permits the computation of a backward-time FTLE through the use of a negative integration length T. A ridge in such a backward-time FTLE field (which we distinguish from forward-time FTLE ridges with the names *attracting LCS* for the former, *repelling LCS* for the latter) corresponds to the time-dependent analogue of an unstable manifold. A symmetry in the ER3BP equations of motion, akin to the CR3BP symmetry described previously, eliminates the need to compute backward-time FTLE fields: noting that the cosine function is an even function, it is easy to check that the mapping $(x, y, x', y', f) \mapsto (x, -y, -x', y', -f)$ is a symmetry of equations (8-9); as a result, any attracting LCS in the ER3BP can be found by negating the y and x' coordinates of every point on the corresponding repelling LCS and viewing its evolution in reverse time. Moreover, equations (8-9) are periodic with period 2π. Thus, the Lagrangian coherent structures in the ER3BP need only be computed over the interval $0 \leq f < 2\pi$; an LCS at any other epoch f can be identified with the LCS at f modulo 2π.

2 Results

2.1 Computational Methodology

A key obstacle encumbering the investigation of Lagrangian coherent structures (LCS) in the elliptic restricted three-body problem (ER3BP) is the dimension of the system under examination. In contrast to the CR3BP, where the existence of a constant of motion restricts the motion of the test particle to a three-dimensional energy surface within which there exist cylindrical invariant manifolds, the ER3BP has a four-dimensional phase space and possesses no integrals of motion. Thus, any LCS in the ER3BP is formally a three-dimension surface contained in $\mathbb{R}^4$. As an extraction and visualization of such a structure would be difficult, we shall explore two means of circumventing this obstacle.

2.1.1 Poincaré Maps and the Finite-Iteration Lyapunov Exponent

One such method utilizes Poincaré sections to reduce the dimension of the system by one. Selecting a three-dimensional hyperplane $U \subset \mathbb{R}^4$ and seeding a subset $U_0 \subset U$ with a grid of tracers, we can advect these

tracers under the flow until the their orbits' (directed) N^{th} intersections with the hyperplane are reached. It then becomes feasible to compute a finite-iteration Lyapunov exponent (FILE)

$$\sigma^N(\mathbf{x}) = \frac{1}{|N|} \ln \left\| \frac{d\mathbf{P}^N(\mathbf{x})}{d\mathbf{x}} \right\|, \tag{15}$$

for each point $\mathbf{x} \in U_0$, where the function $\mathbf{P} : U \to U$ is the one-sided Poincaré map associated with the plane U and the flow Φ of equations (8-9). We shall refer to this method as the Poincaré map method, its associated field being an FILE field.

2.1.2 The Finite-Time Lyapunov Exponent

The second method is more conventional. To motivate the nomenclature adopted here, observe that the matrix $\frac{d\Phi_{t_0}^{t_0+T}(\mathbf{x})}{d\mathbf{x}}$ belonging to the FTLE expression (13) at a given point consists of partial derivatives of the form $\frac{\partial[\Phi_{t_0}^{t_0+T}(\mathbf{x})]_i}{\partial x_j}$, where x_i and x_j are two (possibly identical) components of the state vector $\mathbf{x}$. For the purposes of LCS computation, calculation of these partial derivatives involves central differencing of neighboring tracers separated by an initial deviation $\Delta \mathbf{x}_j = (0, \ldots, 0, \Delta x_j, 0, \ldots, 0)$ in the $\hat{x}_j$ direction[3]:

$$\frac{\partial[\Phi_{t_0}^{t_0+T}(\mathbf{x})]_i}{\partial x_j} \approx \frac{[\Phi_{t_0}^{t_0+T}(\mathbf{x} + \Delta \mathbf{x}_j)]_i - [\Phi_{t_0}^{t_0+T}(\mathbf{x} - \Delta \mathbf{x}_j)]_i}{2\Delta x_j} \tag{16}$$

For this reason, one typically advects a regularly spaced n-dimensional grid of tracers, with at least three tracers along each direction, to compute Lagrangian coherent structures in an n-dimensional dynamical system. Moreover, we deliberately neglect to compute FTLE values at the outermost faces of the cuboidal grid due the absence of adjacent tracers in the outer direction along these faces[2]. This gives rise to the following procedure in the ER3BP, a four-dimensional dynamical system: compute the FTLE field for a four-dimensional grid in the standard manner, setting the width of the grid along one of its axes to be small enough that only three adjacent three-dimensional subgrids are needed to saturate the full grid. In this manner, we obtain a three-dimensional cross-section (the central subgrid) of the four-dimensional FTLE field. Any LCS extracted from this field is a two-dimensional surface that can be visualized graphically. We shall refer to this method as the "three adjacent subgrids" method, its associated field being an FTLE field.

2.1.3 A Comparison Using the Circular Restricted Three-Body Problem (CR3BP) as a Test Bed

In order to gauge the performance of these two methods, we shall first apply them to a simpler, lower dimensional system, namely the CR3BP equations of motion with a fixed energy E. Since the invariant manifolds of the CR3BP are examined in considerable detail in Koon *et al.*[4], it helps to compare the outputs of the two methods with published data. Fig. 6, taken from Koon *et al.*[4], shows the intersection of the stable and unstable manifold tubes of the Lyapunov orbit about L_1 for a fixed energy just above $E(L_1)$. Throughout this report, we adopt the notation of Koon and co-authors[4]: $W_{L_1,\text{p.o.}}^s$ and $W_{L_1,\text{p.o.}}^u$ denote the stable and unstable manifolds, respectively, of the L_1 Lyapunov orbit, and $\Gamma_i^{s,\text{S}}$ and $\Gamma_i^{u,\text{S}}$ denote the ith intersection of $W_{L_1,\text{p.o.}}^s$ and $W_{L_1,\text{p.o.}}^u$, respectively, with the plane $y = 0$ in the interior region within a surface of constant energy. (The capital S in $\Gamma_i^{s,\text{S}}$ specifies that this intersection lies in the interior, or "Sun", region.)

Fig. 7(a) plots the CR3BP FTLE field along the plane $y = 0$ (within a surface of constant energy) for an integration time $T = 2$, as computed using the "three adjacent subgrids" method. As expected, large FTLE values can be observed at the first intersection $\Gamma_1^{s,\text{S}}$ of the stable manifold $W_{L_1,\text{p.o.}}^s$ of the L_1 Lyapunov orbit. Increasing the integration time T (Fig. 7(b)) unveils the subsequent intersection $\Gamma_2^{s,\text{S}}$ of the same stable manifold.

For comparison, the FILE field for the first three iterations of the Poincaré map associated with the plane $y = 0$ (within a surface of constant energy) are shown in Fig. 8. In analogy with increasing integration time, increasing the iteration number N successively unveils the higher order intersections $\Gamma_1^{s,\text{S}}$, $\Gamma_2^{s,\text{S}}$, and $\Gamma_3^{s,\text{S}}$ of $W_{L_1,\text{p.o.}}^s$ with the plane $y = 0$.

---

[2]In reality, one could implement one-sided differencing where necessary to include these outermost faces; in this study, we choose not to for simplicity and assurance of accuracy.
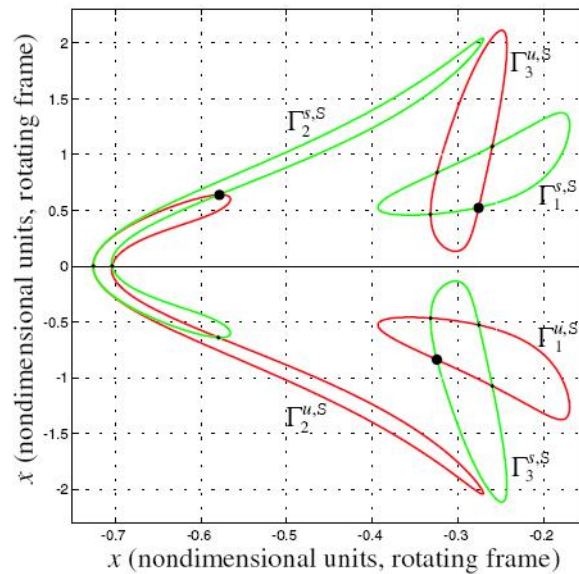
Figure 6: Intersection of the stable (green) and unstable (red) manifold tubes in the CR3BP with the plane $y = 0$ (within a surface of constant energy). Here $\mu = 0.1$ and $E = E(L_1) + .03715$. Subscripts denote the order of intersection of the manifolds with the plane. Image borrowed from Koon *et al.*[4]
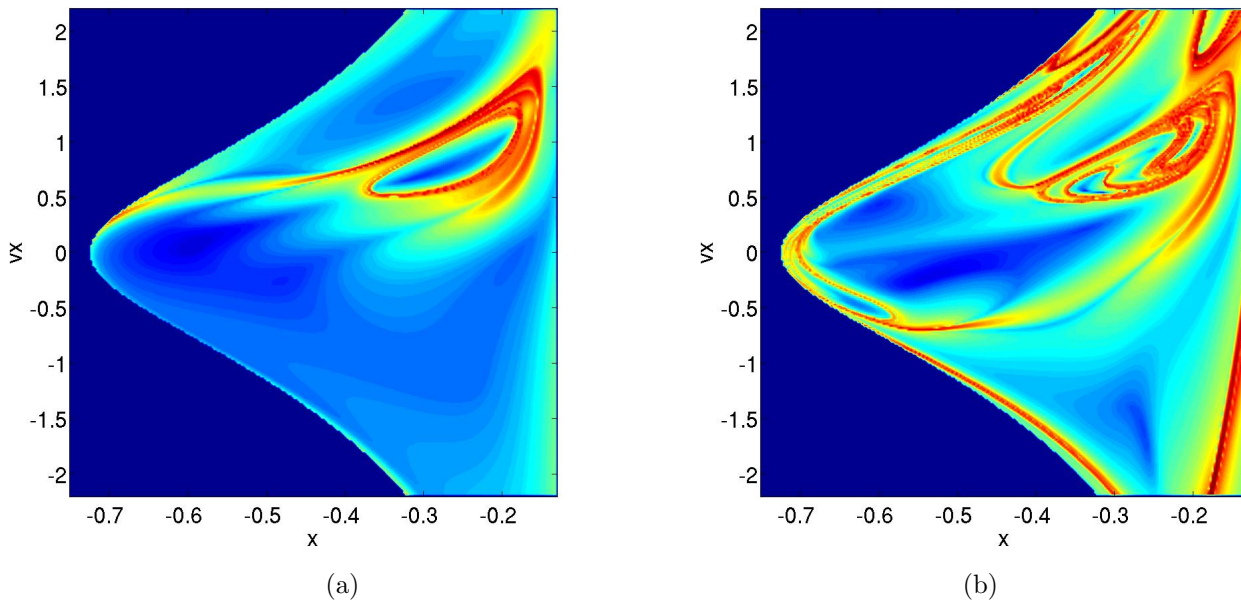

(a)

(b)

Figure 7: FTLE field contour plot (i.e., generated using a "three adjacent subgrids" calculation) in the CR3BP (within a surface of constant energy) at the plane $y = 0$ with integration time (a) $T = 2$ and (b) $T = 5$. Energy and mass parameters are identical to those in Fig. 6. Observe that increasing integration time reveals the second intersection $\Gamma_2^{s,S}$ of the stable manifold of the L_1 Lyapunov orbit, as well as some additional curves of high FTLE.
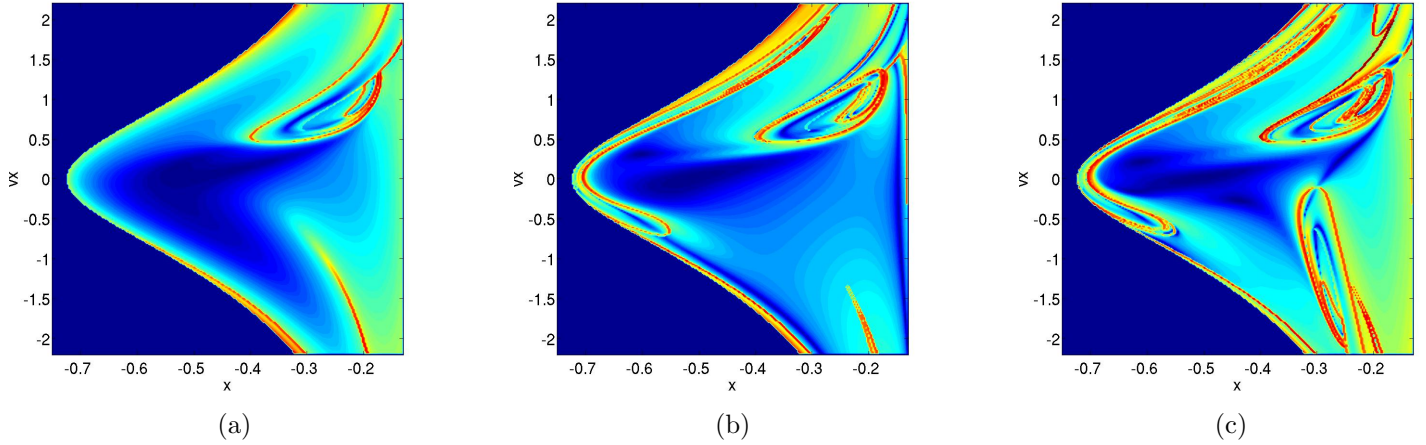
Figure 8: FILE field contour plot (i.e., generated using a Poincaré map calculation) in the CR3BP (within a surface of constant energy) at the plane $y = 0$ for iterations (a) $N = 1$, (b) $N = 2$, and (c) $N = 3$. Again, energy and mass parameters are identical to those in Fig. 6. Notice the superfluous FILE ridges caused by a lack of transversality between orbits and the surface of section in, for instance, the lower right-hand corners of (a) and (b). Unsurprisingly, larger iteration numbers N reveal the higher order intersections $\Gamma_2^{s,\mathrm{S}}$ and $\Gamma_3^{s,\mathrm{S}}$ of the stable manifold of the L_1 Lyapunov orbit.

Notice that the FILE field has a significant drawback: in addition to locating transport barriers associated with stable manifolds of limit sets, the FILE field also exhibits ridges where the Poincaré map is not differentiable due to a lack of transversality between orbits and the plane of interest. Indeed, for initial points on the Poincaré section whose orbits do not intersect the surface of section transversally upon their return, differentiabilty is not guaranteed and the FILE loses its meaning. Unfortunately, for a given FILE field, these structures appear indistinguishably from genuine transport barriers and bear little or no influence on the dynamics of the system. Furthermore, the Poincaré map $\mathbf{P}$ is in general only defined for a subset of the surface of section U; this property can be particularly problematic in the ER3BP, where the absence of energetically forbidden regions permits more frequent orbital escapes. For these reasons, we shall adopt the "three adjacent subgrids" as the standard for all future computations, and shall discard the Poincaré map method.

2.2   Lagrangian Coherent Structures (LCS) in the Elliptic Restricted Three-Body Problem (ER3BP)

The computational tools developed in the previous section make possible the presentation of the main results of this study, Lagrangian coherent structures (LCS) in the elliptic restricted three-body problem (ER3BP). Recall that in the ER3BP, whose equations of motion are non-autonomous and possess no integrals of motion, the notions of constant-energy surfaces lose their relevance, and hence we must examine the time-dependent analogues of $W_{L_1,\mathrm{p.o.}}^s$ and $W_{L_1,\mathrm{p.o.}}^u$ in the full four-dimensional phase space, where the plane $y = 0$ is three-dimensional. An important question to ask at this moment is the following: What will the intersection of $W_{L_1,\mathrm{p.o.}}^s$ with plane $y = 0$ in the interior region look like? The answer to this question depends crucially on our choice of coordinate system.

Let

$$E(x, y, x', y') = \frac{1}{2}(x'^2 + y'^2) - \Omega/(1 + e \cos f), \tag{17}$$

where, in the notation mentioned previously, x' and y' have been used to denote the quantities $\frac{dx}{df}$ and $\frac{dy}{df}$, respectively. Notice that when $e = 0$, (17) reduces to the expression for the energy in the CR3BP given in equation (4). We shall refer to this quantity as the "energy" in the ER3BP, with the hopes that this notation will give the reader a better sense of the correlation between the quantities defined here and their CR3BP analogues. In actuality, (17) is the ER3BP's Hamiltonian; see Section 3 for details.
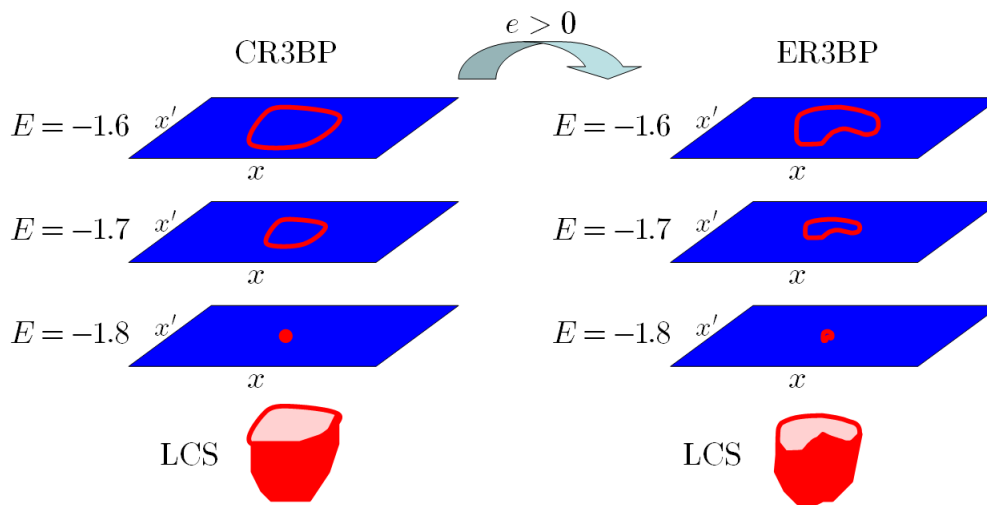
Figure 9: Illustration of the hypothesis that, in terms of the coordinates x, y, x', and E, the intersection of the plane $y = 0$ with the LCS corresponding to the analogue of $W^s_{L_1,\text{p.o.}}$ might appear as a distorted paraboloid in the ER3BP.

Choosing a coordinate system (x, y, x', E) to parametrize phase space in the ER3BP (so that the plane $y = 0$ is parametrized by x, x', and E) allows for a natural means of extending the qualitative results of LCS studies in the CR3BP. For fixed values of E at the plane $y = 0$, $x < 0$, a ridge in the FTLE field on the $(x, x', y = 0, E = const.)$ plane should appear as a closed curve, corresponding to a perturbed version of $\Gamma_1^{s,S}$ (the perturbation arising from the fact that the eccentricity e is nonzero). Since the amplitude of an L_1 Lyapunov orbit in the CR3BP is roughly proportional to the square root of its energy minus $E(L_1)$, we should expect that this closed curve will shrink with decreasing E and that for some critical energy the curve will contract to a point. Consequently, the intersection of the LCS with the plane $y = 0$ might appear as a distorted paraboloid, provided we parametrize phase space with the coordinates x, y, x', and E. See Fig. 9 for an illustration of this notion.

2.2.1   A Test Case

Appendix Figs. 10-11 display the intersection of the plane $y = 0$ with the LCS corresponding to the analogue of $W^s_{L_1,\text{p.o.}}$ under a set of fabricated parameters (mass ratio $\mu = 0.1$, orbital eccentricity $e = 0.04$). The video LCS-ER3BP.mov shows the same images in animated format. The LCS was extracted from an FTLE field generated by advecting tracers over an integration length $T = 2.5$, roughly $\frac{2}{5}$ of the orbital period of the two primary masses. As expected, the LCS forms a distorted paraboloid that pulsates with time. The key property of this LCS is that, like $W^s_{L_1,\text{p.o.}}$ of the CR3BP, this LCS separates orbits that enter m_2's "sphere of influence" from orbits that do not. In contrast to the CR3BP, however, a particle need not be within the LCS "bowl" in order to exit the interior region; the absence of forbidden regions allows orbits to escape the interior region without necessarily ever entering the m_2 region.

To help visualize the role that this LCS plays in the dynamics of the ER3BP, Appendix Figs. 12-13 display snapshots of the motion of a collection of tracers that have been colored based upon their initial location relative to the LCS. The tracers were seeded at true anomaly $f = \pi/2$ over a $15 \times 15 \times 15$ (x, x', E) grid on the plane $y = 0$ and advected forward in time. Blue tracers began inside the LCS "bowl", while red tracers began outside the LCS "bowl". The video Tracers.avi shows the same images in animated format.

2.2.2   LCS in the Earth-Moon System

The Earth-Moon-spacecraft system (mass ratio $\mu \approx 0.012$, orbital eccentricity $e \approx 0.055$) provides an excellent physical system for which ER3BP LCSs can be examined. In this case (see Appendix Figs. 14-15 and the video LCS-ER3BP-Earth-Moon.mov), the intersection of the plane $y = 0$ with the LCS corresponding

to the analogue of $W^s_{L_1,\text{p.o.}}$ is smaller than in the case above, which is to be expected given the lower mass ratio μ in the Earth-Moon system. It is also evident that this LCS is not as clean than in the case above, perhaps owing to integration error or to a genuine decay in the precision of the boundary separating transit orbits from non-transit orbits.

2.2.3   Remarks

One of the original goals of this study involved computation of Lagrangian coherent structures in the Sun-Mercury-spacecraft system (mass ratio $\mu \approx 1.7 \times 10^{-7}$, eccentricity $e \approx 0.21$), in the hopes that applying these methods to a planet with a notably high orbital eccentricity might illustrate their importance most vividly. This endeavor has been abandoned for several reasons. Most importantly, numerical experiment suggests that the CR3BP μ-dependent energy difference $\Delta E = -\frac{3}{2} - E(L_1)$ provides a good gauge of the width of the energy range over which an LCS like the one studied in the above two cases is likely to be found in an ER3BP system with the same μ. To rationalize this observation, note that when $E < E(L_1)$ in the CR3BP, the interior and m_2 regions are not connected; on the other hand, when $E > -\frac{3}{2}$ the entire (x, y) plane is accessible. For the Sun-Mercury mass ratio, $\Delta E \approx 7 \times 10^{-5}$; from a practical perspective, such an energy range is disappointingly small. Furthermore, globalization of the CR3BP invariant manifolds for $\mu \approx 1.7 \times 10^{-7}$ and $E(L_1) < E < -1.5$ reveals that $W^s_{L_1,\text{p.o.}}$ adopts a considerably long and intricate path before reaching the plane $y = 0$ in the interior region. Assuming the analogous Sun-Mercury LCS takes a similar form, this implies that a large integration length T would be needed to perform a relevant FTLE calculation. On the other hand, studying, for instance, the plane $x = 1 - \mu$ in the m_2 region of the Sun-Mercury system requires tight integration thresholds to deal with the proximity to m_2 of LCSs in that region, where collision-bound orbits are ubiquitous.

3   Conclusions and Further Study

The results presented in this report demonstrate the existence of periodically pulsating Lagrangian coherent structures in the phase space of the elliptic restricted three-body problem which arise as the time-dependent analogues of stable and unstable manifolds of periodic orbits in the circular restricted three-body problem. The examination of cross-sections of full-dimensional finite-time Lyapunov exponent fields proves to be an effective method of computing the intersections of these structures with surfaces of section in the ER3BP phase space, whose high dimension precludes the visualization of entire LCSs. As a concrete application, these results reveal the influence of orbital eccentricity on segments of the Interplanetary Transport Network associated with elliptically orbiting mass pairs.

Interestingly, LCS pulsation in the cases presented is characterized almost entirely by sinusoidal translation in E. An analytical explanation of this observation seems a worthy topic for further study. In addition, an investigation of the dual role that these structures play as both separatrices and as the invariant manifolds of quasiperiodic orbits deserves consideration; an interesting, albeit unsurprising, phenomenon is the observation that any tracer that lies on an ER3BP LCS eventually tends toward a quasiperiodic orbit.

From a computational perspective, ridge extraction from three-dimensional FTLE fields presents a formidable challenge in a study such as this. The design of an automated ridge extraction algorithm for arbitrary-dimensional scalar fields would constitute an enormous advancement for the LCS community.

The use of a symplectic integrator would also benefit this study, as the ER3BP is a Hamiltonian system: let $p_x = \frac{dx}{df} - y$, $p_y = \frac{dy}{df} + x$, and $H(x, y, p_x, p_y, f) = \frac{1}{2}((p_x + y)^2 + (p_y - x)^2) - \Omega/(1 + e \cos f)$. Then equations (8-9) take the form

$$
\begin{aligned}
\frac{dx}{df} &= \frac{\partial H}{\partial p_x} \\
\frac{dy}{df} &= \frac{\partial H}{\partial p_y} \\
\frac{dp_x}{df} &= -\frac{\partial H}{\partial x} \\
\frac{dp_y}{df} &= -\frac{\partial H}{\partial y}
\end{aligned}
\tag{18}
$$

It is well known [14] that the flow of a Hamiltonian dynamical system is symplectic, i.e. the matrix $\frac{d\Phi_{t_0}^{t_0+T}(\mathbf{x})}{d\mathbf{x}}$ of (13) satisfies $\frac{d\Phi_{t_0}^{t_0+T}(\mathbf{x})}{d\mathbf{x}}^* J \frac{d\Phi_{t_0}^{t_0+T}(\mathbf{x})}{d\mathbf{x}} = J$ for all integration lengths T, where J is the $2n \times 2n$ matrix

$$J = \begin{pmatrix} 0 & I_n \\ -I_n & 0 \end{pmatrix} \tag{19}$$

and n is the number of degrees of freedom of the system at hand (in our case, $n = 2$). Symplectic integrators respect this property [15]; general integration schemes like the Runge-Kutta method used in this study do not. Consequently, an intrinsic layer of structure associated with the ER3BP equations of motion has been implicitly ignored through the use of a non-symplectic integration scheme.

4   Methods

For brevity, a few details concerning the three-body-problem equations of motion and LCS computations have been omitted from the previous sections. We present them here for completeness.

4.1   Derivation of the ER3BP Equations of Motion

In the following, the equations of motion for the elliptic restricted three-body problem are derived using elementary properties of elliptical orbits obtained from the general solution to the two-body problem. A derivation following a similar approach is given in Szebehely [10], where the author proceeds by transforming the equations of motion from the inertial coordinate frame to an intermediate rotating frame and finally to the rotating, pulsating frame in which the equations of motion have the simplest form.

Let $m_1 = 1 - \mu$ and $m_2 = \mu$ be two masses in elliptical orbit about their center of mass. Let e and $f(t)$ be the mutual eccentricity and true anomaly of these two primary masses' elliptical orbits, and let $r(f)$ be the distance between these two masses. Normalize units so that the pair of primary masses has unit angular momentum and $r(\frac{\pi}{2}) = 1$. Elementary results on the solution to the two-body problem give the following relations between r, f, and their derivatives:

$$r(f) = \frac{1}{1 + e \cos f} \tag{20}$$

$$r^2 \dot{f} = 1 \tag{21}$$

$$\ddot{r} = r\dot{f}^2 - \frac{1}{r^2} \tag{22}$$

Equation (20) is simply the equation for an ellipse with unit semi-latus rectum in polar coordinates, (21) follows from conservation of angular momentum, and (22) represents the two-body problem equations of motion in polar coordinates. Differentiating (21) with respect to time and solving for $\dot{r}$ gives

$$\dot{r} = -\frac{r\ddot{f}}{2\dot{f}} \tag{23}$$

Utilizing (21), we can recast (22) and (23) as

$$\dot{r} = -\frac{1}{2}r^3\ddot{f} \tag{24}$$

$$\ddot{r} = \frac{1}{r^3} - \frac{1}{r^2}. \tag{25}$$

These two expressions for $\dot{r}$ and $\ddot{r}$ will come in handy in our derivation of the ER3BP equations of motion.

Let (x, y) denote the position of the test mass m_3 with respect to the nonuniformly rotating, isotropically pulsating, barycentric coordinate frame described in Section 1.1.2. In this coordinate frame, the primary masses m_1 and m_2 have fixed positions $(-\mu, 0)$ and $(1 - \mu, 0)$, respectively; hence, any distance a given in this frame corresponds to an (inertial frame) distance $ar(f)$, where $r(f)$ is the instantaneous (inertial frame)

distance between m_1 and m_2. Represent the position (x, y) with the complex vector $\xi = x + iy$, and let z denote the complex position of m_3 with respect to the inertial, barycentric frame whose axes coincide with those of the rotating, pulsating frame at $f = 0$. Then we have

$$z = \xi r \exp(if). \tag{26}$$

Now let r_{13} and r_{23} denote the complex (non-pulsated) vectors joining the primary masses m_1 and m_2, respectively, to the test mass m_3, as in Fig. 1. Newton's second law, together with the fact that gravitational forces follow an inverse square law, then gives

$$
\begin{aligned}
\ddot{z} &= \left(-\frac{\mu r_{23}}{|r_{23}|^3} - \frac{(1-\mu)r_{13}}{|r_{13}|^3} \right) \exp(if) \\
&= \left(-\frac{\mu(\xi - 1 + \mu)r}{|(\xi - 1 + \mu)r|^3} - \frac{(1-\mu)(\xi + \mu)r}{|(\xi + \mu)r|^3} \right) \exp(if) \\
&= \left(-\frac{\mu(\xi - 1 + \mu)}{|\xi - 1 + \mu|^3} - \frac{(1-\mu)(\xi + \mu)}{|\xi + \mu|^3} \right) \frac{\exp(if)}{r^2},
\end{aligned}
\tag{27}
$$

where we have expressed inertial frame forces in terms of the rotating, pulsating coordinate $\xi = x + iy$ by scaling distances by r and transforming to the non-rotating frame through multiplication by $\exp(if)$. For brevity, let

$$F(\xi) = -\frac{\mu(\xi - 1 + \mu)}{|(\xi - 1 + \mu)|^3} - \frac{(1-\mu)(\xi + \mu)}{|(\xi + \mu)|^3} \tag{28}$$

so that equation (27) becomes

$$\ddot{z} = \exp(if)\frac{F(\xi)}{r^2}. \tag{29}$$

Using the relation given in (26) to expand the left hand side of (29), we have

$$\exp(if)\frac{F(\xi)}{r^2} = \exp(if)(\ddot{r}\xi + 2\dot{r}\dot{\xi} + 2i\dot{f}\dot{r}\xi + 2i\dot{f}r\dot{\xi} + r\ddot{\xi} + i\ddot{f}r\xi - \dot{f}^2 r\xi).$$

Multiplying through by $r^3 \exp(-if)$ gives

$$rF(\xi) = r^3\ddot{r}\xi + 2r^3\dot{r}\dot{\xi} + 2i\dot{f}r^3\dot{r}\xi + 2i\dot{f}r^4\dot{\xi} + r^4\ddot{\xi} + i\ddot{f}r^4\xi - \dot{f}^2 r^4\xi.$$

We are now in a position to utilize the expressions for $\dot{r}$ and $\ddot{r}$ given in (24-25), along with the identity (21):

$$
\begin{aligned}
rF(\xi) &= \xi - r\xi - \ddot{f}r^6\dot{\xi} - i\dot{f}\ddot{f}r^6\xi + 2ir^2\dot{\xi} + r^4\ddot{\xi} + i\ddot{f}r^4\xi - \xi \\
&= -r\xi - \ddot{f}r^6\dot{\xi} + 2ir^2\dot{\xi} + r^4\ddot{\xi}
\end{aligned}
$$

In order to use f as our independent variable, we must write down the relations between the derivatives of ξ with respect to f and t using the chain rule:

$$
\begin{aligned}
\dot{\xi} &= \frac{d\xi}{df}\dot{f} \tag{30} \\
\ddot{\xi} &= \frac{d^2\xi}{df^2}\dot{f}^2 + \frac{d\xi}{df}\ddot{f} \tag{31}
\end{aligned}
$$

We then have

$$
\begin{aligned}
rF(\xi) &= -r\xi - \ddot{f}r^6\frac{d\xi}{df}\dot{f} + 2ir^2\frac{d\xi}{df}\dot{f} + r^4\left(\frac{d^2\xi}{df^2}\dot{f}^2 + \frac{d\xi}{df}\ddot{f}\right) \\
&= -r\xi - \ddot{f}r^4\frac{d\xi}{df} + 2i\frac{d\xi}{df} + \frac{d^2\xi}{df^2} + r^4\frac{d\xi}{df}\ddot{f} \\
&= -r\xi + 2i\frac{d\xi}{df} + \frac{d^2\xi}{df^2} \\
(\xi + F(\xi))r &= \frac{d^2\xi}{df^2} + 2i\frac{d\xi}{df}, \tag{32}
\end{aligned}
$$

where once again we have utilized the identity $r^2\dot{f} = 1$. Equating the real and imaginary parts of the two sides of (32) and substituting the expressions for $r(f)$ and $F(\xi)$ given in (20) and (28) yields the equations of motion for the elliptic restricted three-body problem:

$$\frac{d^2x}{df^2} - 2\frac{dy}{df} = \left(x - \frac{\mu(x-1+\mu)}{((x-1+\mu)^2+y^2)^{3/2}} - \frac{(1-\mu)(x+\mu)}{((x+\mu)^2+y^2)^{3/2}}\right)\Big/(1+e\cos f) \tag{33}$$

$$\frac{d^2y}{df^2} + 2\frac{dx}{df} = \left(y - \frac{\mu y}{((x-1+\mu)^2+y^2)^{3/2}} - \frac{(1-\mu)y}{((x+\mu)^2+y^2)^{3/2}}\right)\Big/(1+e\cos f), \tag{34}$$

or, more concisely,

$$\frac{d^2x}{df^2} - 2\frac{dy}{df} = \frac{\partial\Omega}{\partial x}\Big/(1+e\cos f) \tag{35}$$

$$\frac{d^2y}{df^2} + 2\frac{dx}{df} = \frac{\partial\Omega}{\partial y}\Big/(1+e\cos f), \tag{36}$$

where

$$\Omega(x,y) = \frac{x^2+y^2}{2} + \frac{1-\mu}{\sqrt{(x+\mu)^2+y^2}} + \frac{\mu}{\sqrt{(x-1+\mu)^2+y^2}} + \frac{1}{2}\mu(1-\mu). \tag{37}$$

Notice that when $e = 0$, $\frac{df}{dt} = 1$ so that $f = t$ and equations (35-36) reduce to

$$\frac{d^2x}{dt^2} - 2\frac{dy}{dt} = \frac{\partial\Omega}{\partial x} \tag{38}$$

$$\frac{d^2y}{dt^2} + 2\frac{dx}{dt} = \frac{\partial\Omega}{\partial y}, \tag{39}$$

which are the equations of motion for the circular restricted three-body problem.

4.2 Integration and Ridge Extraction

In this study, an adaptive-time stepping Runge-Kutta-Fehlberg routine (RKF45)[16] was used to integrate tracers for the computation of FTLE fields. To extract ridges from three-dimensional FTLE fields, contour plots of two-dimensional slices of each three-dimensional FTLE field were generated. For each slice, the ridge of interest was traced out manually with a sequence of points. A nonuniform rational B-spline (NURBS)[17] surface was then generated using the selected points as control points.

5 References

1. Dellnitz, M. *et al.* Transport in dynamical astronomy and multibody problems. *International Journal of Bifurcation and Chaos* **15**, 699-727 (2005).

2. Porter, M. A. & Cvitanović P. Ground control to Niels Bohr: exploring outer space with atomic physics. *Notices of the American Mathematical Society* **52**, 1020-1025 (2005).

3. Shadden, S. C., Lekien, F. & Marsden, J. E. Definition and properties of Lagrangian coherent structures from finite-time Lyapunov exponents in two-dimensional aperiodic flows. *Physica D* **212**, 271-304 (2005).

4. Koon, W. S., Lo, M., Marsden, J. E. & Ross, S. D. Heteroclinic connections between periodic orbits and resonance transitions in celestial mechanics. *Chaos* **10**, 427-469 (2000).

5. Marsden, J. E. & Ross, S. D. New methods in celestial mechanics and mission design. *Bulletin of the American Mathematical Society* **43**, 43-73 (2005).

6. Koon, W. S., Lo, M. W., Marsden, J. E. & Ross, S. D. Resonance and capture of Jupiter comets. *Celestial Mechanics and Dynamical Astronomy* **81**, 27-38 (2001).

7. Gómez, G., Koon, W. S., Lo, M. W., Marsden, J. E., Masdemont, J. & Ross, S. D. Connecting orbits and invariant manifolds in the spatial restricted three-body problem. *Nonlinearity* **17**, 1571-1606 (2004).

8. Koon, W. S., Lo, M. W., Marsden, J. E. & Ross, S. D. Dynamical systems, the three-body problem, and space mission design. *International Conference on Differential Equations*, Berlin, 1999, (Fiedler, B., Gröger, K. & Sprekels, J. eds.), World Scientific, 1167-1181 (2000).

9. Parker, T. S. & Chua L. O. *Practical Numerical Algorithms for Chaotic Systems*, (Springer-Verlag, New York, 1989).

10. Szebehely, V. G. *Theory of Orbits: The Restricted Problem of Three Bodies*, (Academic Press, New York, 1967).

11. Goldstein, H., Poole, C. & Safko, J. *Classical Mechanics* (Addison Wesley, San Fransisco, 2002).

12. Ross, S. D. "Cylindrical Manifolds and Tube Dynamics in the Restricted Three-Body Problem" (PhD thesis, California Institute of Technology, 2004).

13. Lekien, F., Shadden S. C., & Marsden, J. E. Lagrangian coherent structures in n-dimensional systems. *Journal of Mathematical Physics* **48**, 1-19 (2007).

14. Arnold, V. I. *Mathematical Methods of Classical Mechanics*, (Springer-Verlag, New York, 1989).

15. Marsden, J. E. & West, M. Discrete mechanics and variational integrators. *Acta Numerica* **10**, 357-514 (2001).

16. Press, W. H., Teukolsky, S. A., Vetterling, W. T. & Flannery, B. P. *Numerical Recipes in C: The Art of Scientific Computing*, (Cambridge University Press, New York, 1992).

17. Piegl, L. & Tiller, W. *The NURBS Book* (Springer-Verlag, New York, 1997).
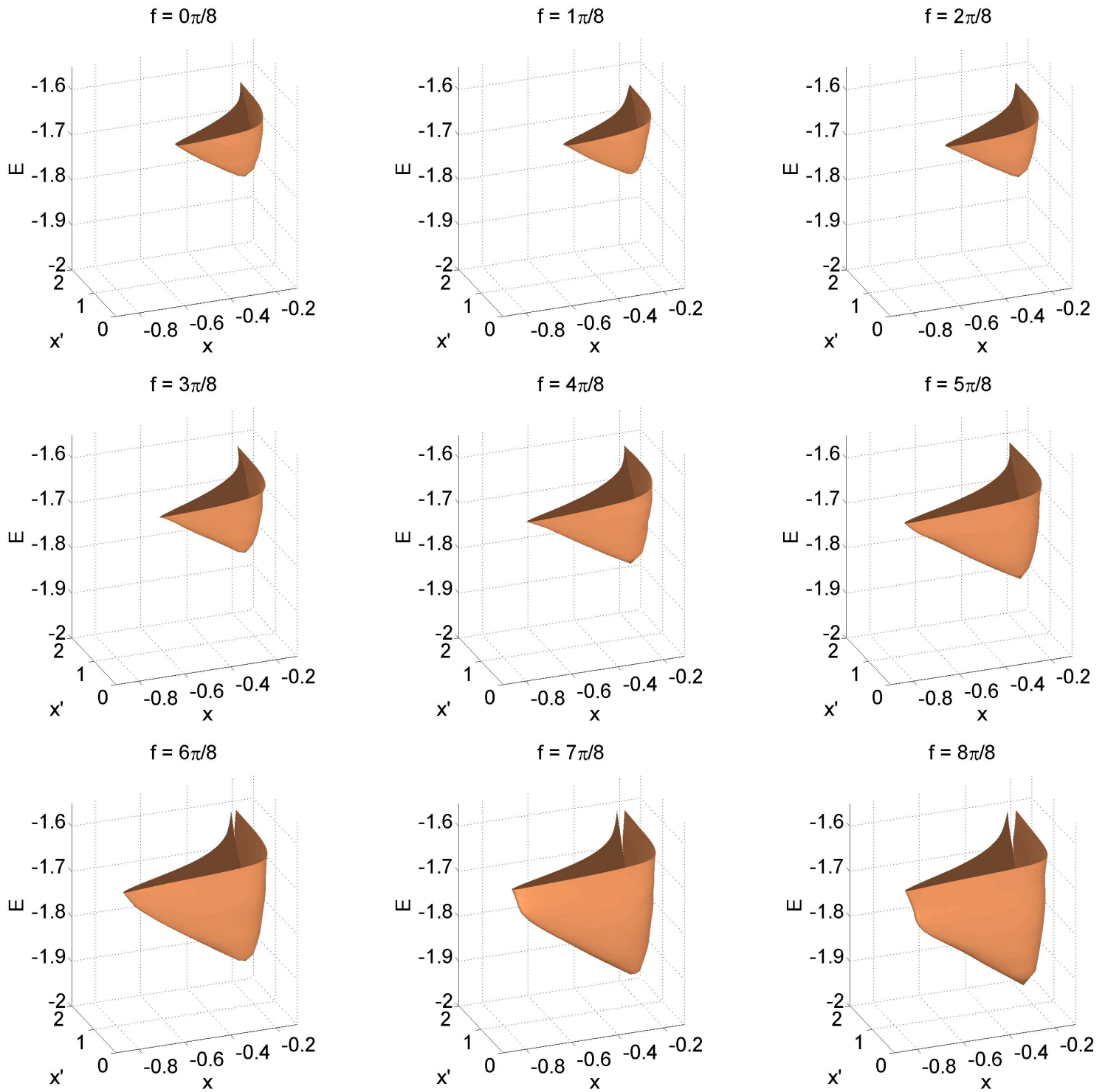
6 Acknowledgments

7 Appendix

Figure 10: Intersection of the plane $y = 0$ with the LCS corresponding to the time-dependent analogue of $W^s_{L_1,\text{p.o.}}$ in the ER3BP with mass ratio $\mu = 0.1$, orbital eccentricity $e = 0.04$. See LCS-ER3BP.mov for an animation.
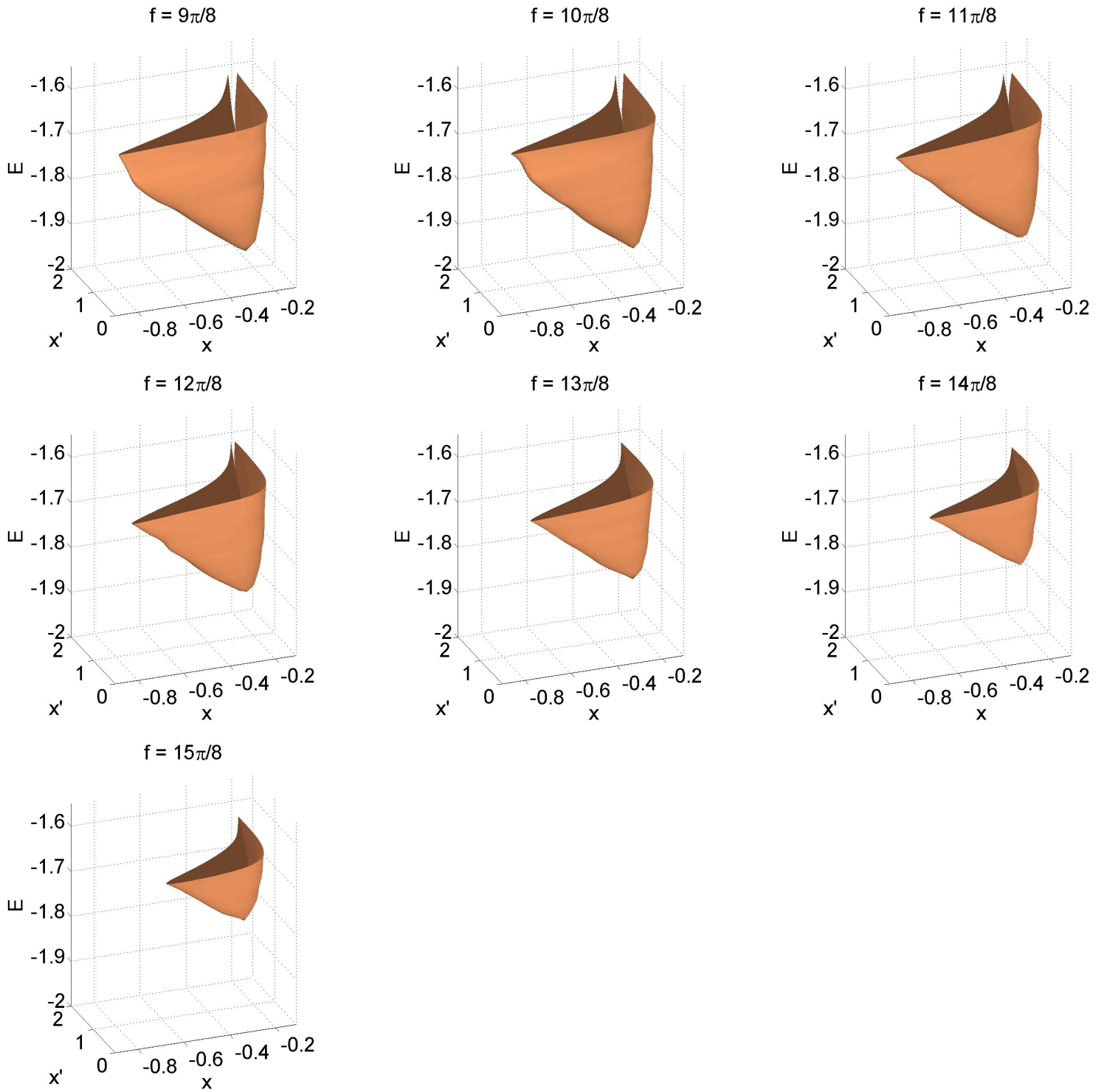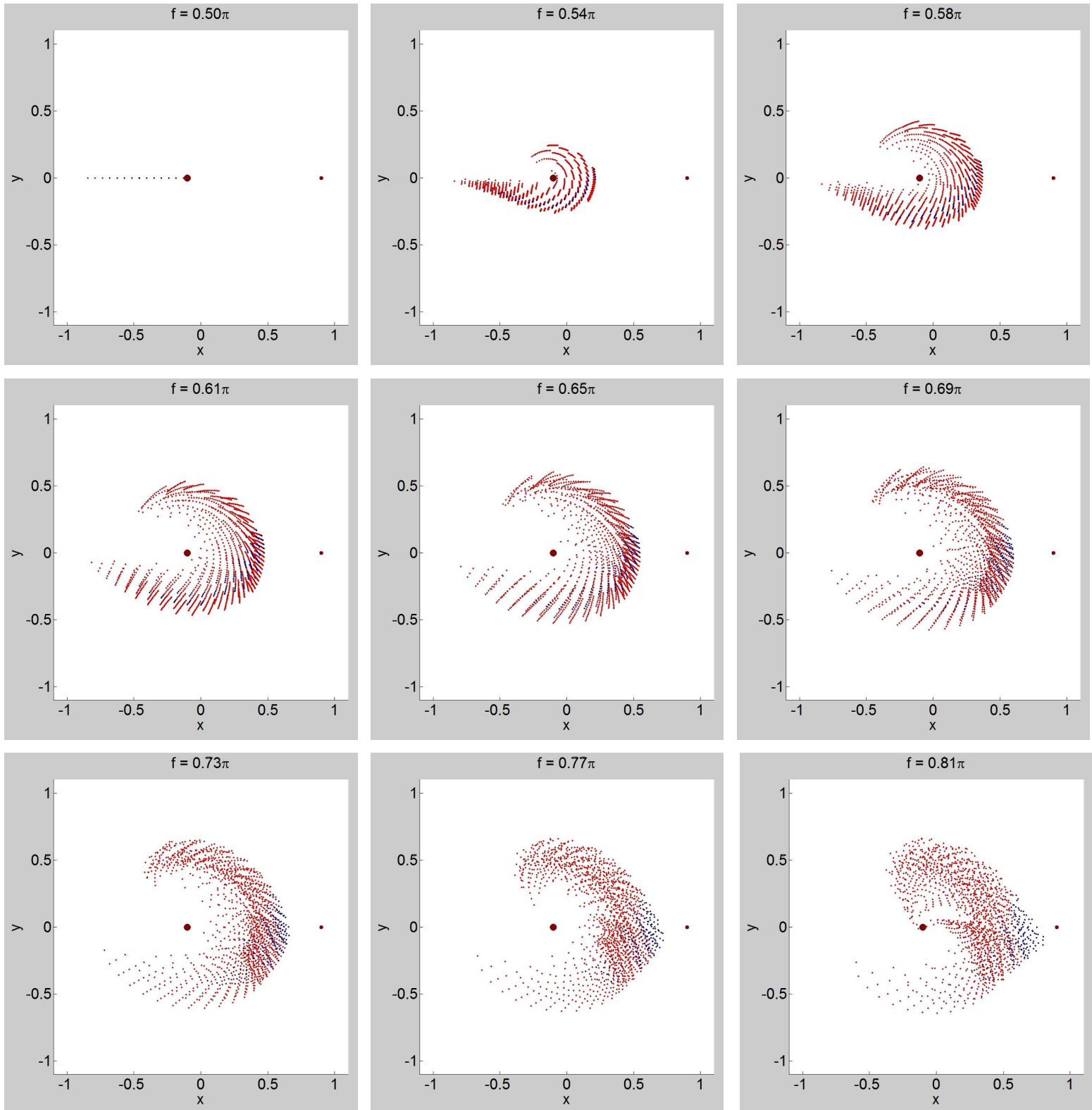
Figure 11: *(continued from previous page)* Intersection of the plane $y = 0$ with the LCS corresponding to the time-dependent analogue of $W^s_{L_1,\text{p.o.}}$ in the ER3BP with mass ratio $\mu = 0.1$, orbital eccentricity $e = 0.04$. See LCS-ER3BP.mov for an animation.

Figure 12: Snapshots of the motion of a collection of tracers colored based upon their initial location relative to the LCS in Appendix Figs. 10-11. The tracers were seeded at true anomaly $f = \pi/2$ over a $15 \times 15 \times 15$ (x, x', E) grid on the plane $y = 0$ and advected forward in time. Blue tracers began inside the LCS "bowl", while red tracers began outside the LCS "bowl". See Tracers.avi for an animation.
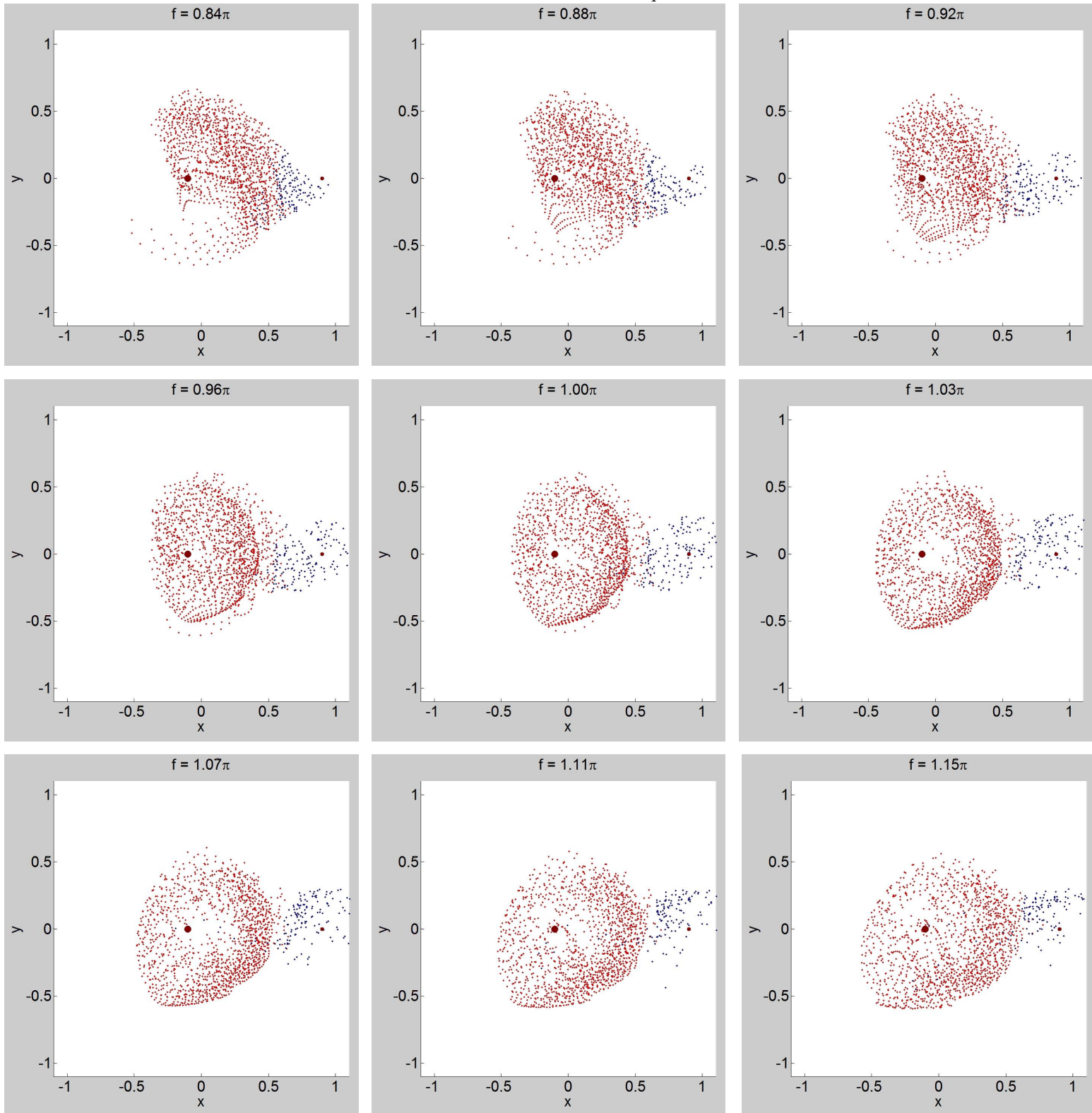
Figure 13: *(continued from previous page)* Snapshots of the motion of a collection of tracers colored based upon their initial location relative to the LCS in Appendix Figs. 10-11. The tracers were seeded at true anomaly $f = \pi/2$ over a $15 \times 15 \times 15$ (x, x', E) grid on the plane $y = 0$ and advected forward in time. Blue tracers began inside the LCS "bowl", while red tracers began outside the LCS "bowl". See Tracers.avi for an animation.
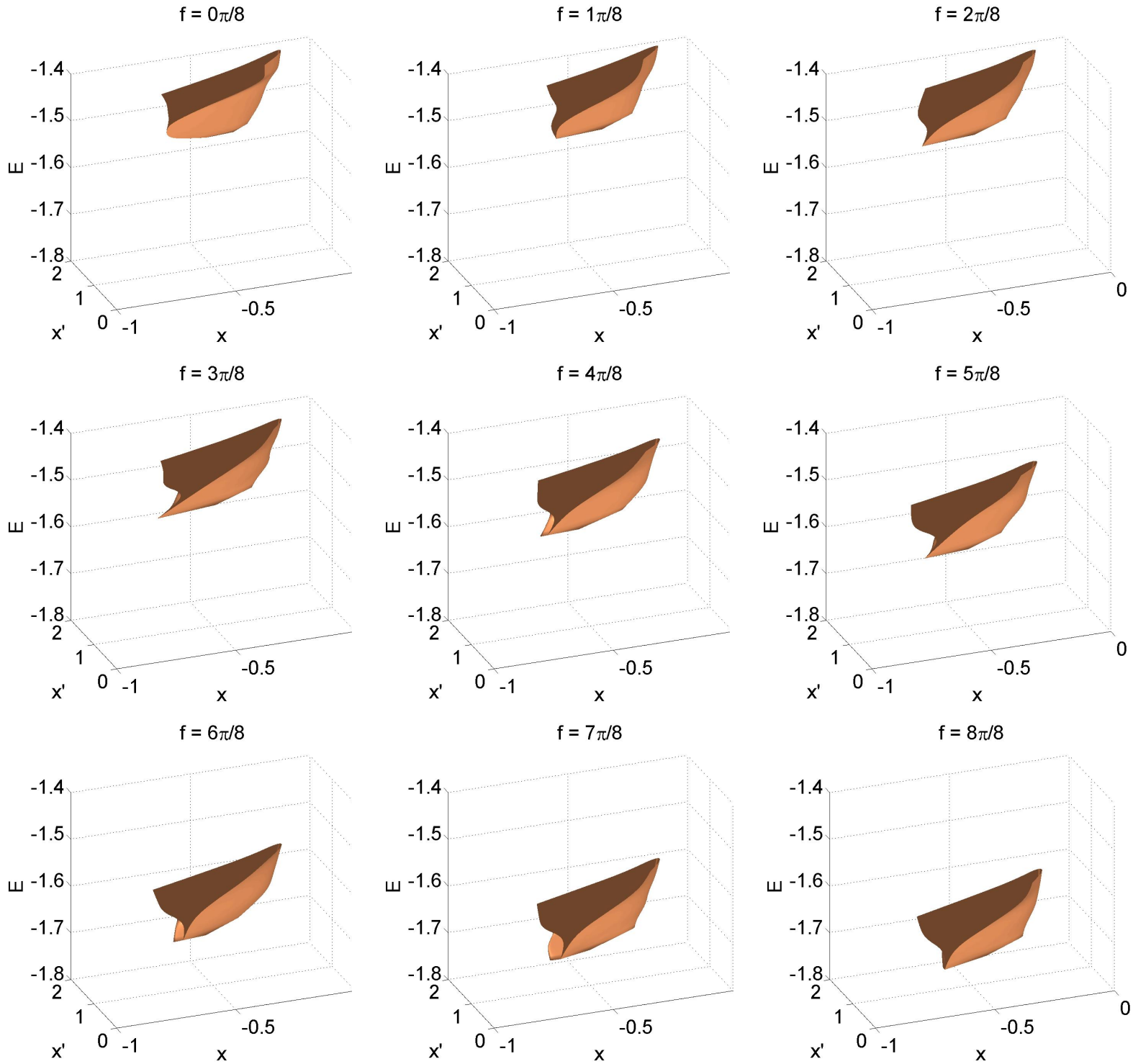
Figure 14: Intersection of the plane $y = 0$ with the LCS corresponding to the time-dependent analogue of $W_{L_1,\text{p.o.}}^s$ in the Earth-Moon-spacecraft system (mass ratio $\mu \approx 0.012$, orbital eccentricity $e \approx 0.055$). See LCS-ER3BP-Earth-Moon.mov for an animation.

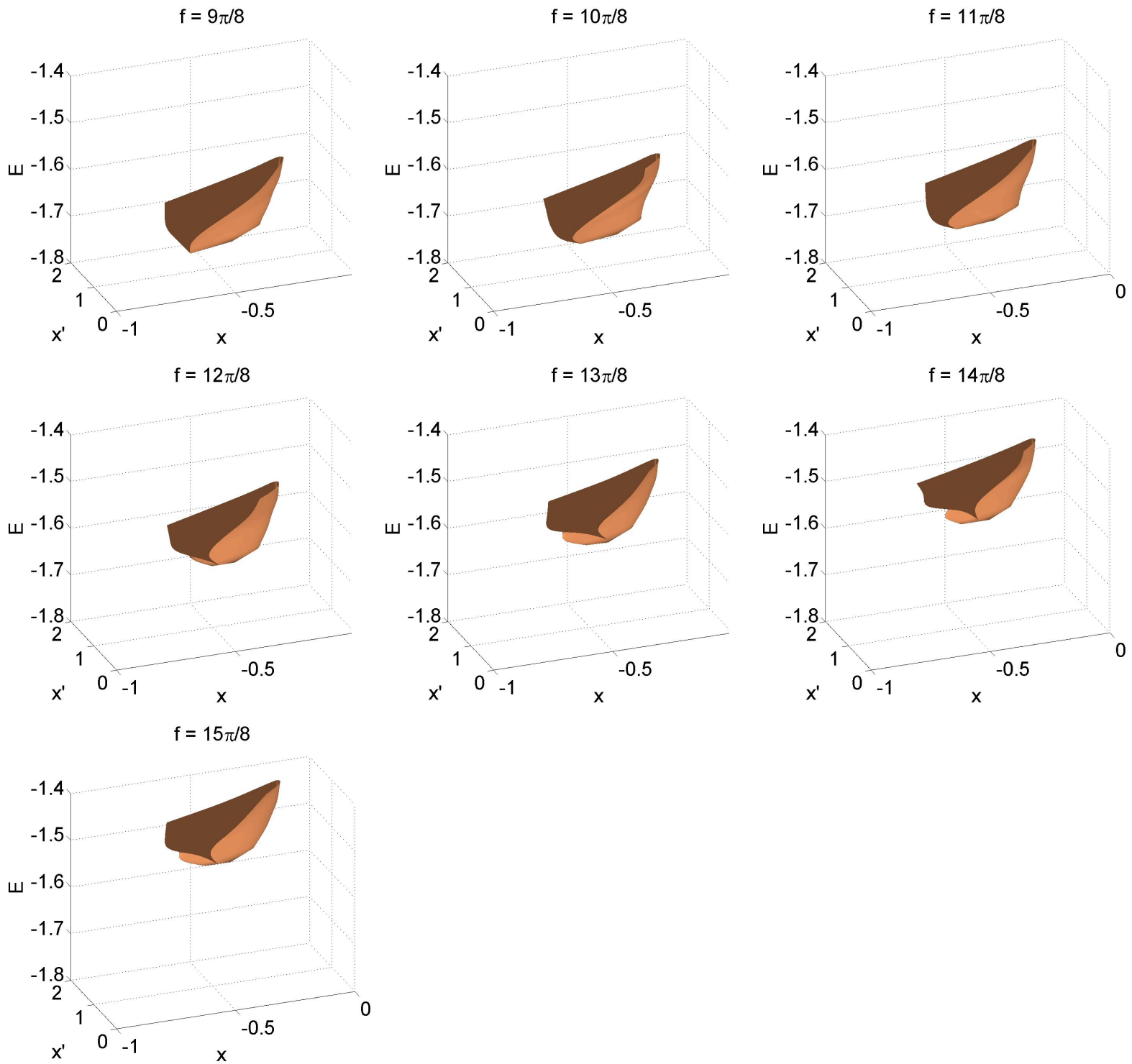Figure 15: *(continued from previous page)* Intersection of the plane $y = 0$ with the LCS corresponding to the time-dependent analogue of $W^s_{L_1,\text{p.o.}}$ in the Earth-Moon-spacecraft system (mass ratio $\mu \approx 0.012$, orbital eccentricity $e \approx 0.055$). See LCS-ER3BP-Earth-Moon.mov for an animation.